Astronomy & Astrophysics manuscript no. cxoshnl
May 9, 2025

Subaru High-z Exploration of Low-Luminosity Quasars (SHELLQs) XXII. Chandra observations of narrow-line quasar candidates at $z \geq 6$

K. Iwasawa[1,2], R. Gilli[3], F. Vito[3], Y. Matsuoka[4], M. Onoue[5,6,7], M. A. Strauss[8], N. Kashikawa[9], Y. Toba[10,11], K. Shimasaku[9], K. Inayoshi[7], T. Nagao[4], N. Kawanaka[12,13], J. D. Silverman[5,6], T. Izumi[13], K. Kohno[14,15], and Y. Ueda[16]

[1] Institut de Ciències del Cosmos (ICCUB), Universitat de Barcelona (IEEC-UB), Martí i Franquès, 1, 08028 Barcelona, Spain
[2] ICREA, Pg. Lluís Companys 23, 08010 Barcelona, Spain
[3] INAF – Osservatorio di Astrofisica e Scienza dello Spazio di Bologna, Via Gobetti 93/3, I-40129 Bologna, Italy
[4] Research Center for Space and Cosmic Evolution, Ehime University, 2-5 Bunkyo-cho, Matsuyama, Ehime 790-8577, Japan
[5] Kavli Institute for the Physics and Mathematics of the Universe (WPI),The University of Tokyo Institutes for Advanced Study, The University of Tokyo, Kashiwa, Chiba 277-8583, Japan
[6] Center for Data-Driven Discovery, Kavli IPMU (WPI), UTIAS, The University of Tokyo, Kashiwa, Chiba 277-8583, Japan
[7] Kavli Institute for Astronomy and Astrophysics, Peking University, Beijing 100871, China
[8] Department of Astrophysical Sciences, Princeton University, 4 Ivy Lane, Princeton, NJ 08544, USA
[9] Department of Astronomy, School of Science, The University of Tokyo, 7-3-1 Hongo, Bunkyo, Tokyo 113-0033, Japan
[10] Department of Physical Sciences, Ritsumeikan University,Kusatsu Shiga 525-8577, Japan
[11] Academia Sinica Institute of Astronomy and Astrophysics, 11F Astronomy-Mathematics Building, AS/NTU, No.1, Section 4, Roosevelt Road, Taipei 10617, Taiwan
[12] Department of Physics, Graduate School of Science Tokyo Metropolitan University, Hachioji-shi, Tokyo 192-0397
[13] National Astronomical Observatory of Japan, Osawa, Mitaka, Tokyo 181-8588, Japan
[14] Institute of Astronomy, Graduate School of Science, The University of Tokyo, 2-21-1 Osawa, Mitaka, Tokyo 181-0015, Japan
[15] Research Center for the Early Universe, Graduate School of Science, The University of Tokyo, Hongo, Tokyo 113-0033, Japan
[16] Department of Astronomy, Kyoto University, Sakyo-ku, Kyoto, Japan

May 9, 2025

ABSTRACT

We report on Chandra X-ray observations of four narrow-line quasar candidates at $z \sim 6$, selected from the SHELLQs project, based on the Subaru Hyper Suprime-Cam survey. These objects are characterised by narrow (FWHM$\leq$ 310 km s^{-1}), luminous ($> 10^{44}$ erg s^{-1}) Lyα and faint UV continuum ($M_{1450} = -22$ - -21), prompting us to examine whether they are obscured luminous AGN at the epoch of reionization. However, none of these objects were detected by Chandra, giving an upper limit to their rest-frame 2-10 keV luminosity (L_X) of 2×10^{44} erg s^{-1} (2σ), assuming a spectral slope $\Gamma = 2$. Subsequent rest-frame optical spectroscopy of these objects by the JWST-NIRSpec, presented in a companion paper, show weak broad Balmer emission at the base of narrow cores. With the scaling relation for low-redshift AGN, the observed strong [OIII]λ5007 flux of these sources would predict L_X to be around 10^{45} erg s^{-1}, which is well above the Chandra upper limits. These optical spectra and X-ray quietness are reminiscent of JWST-selected broad-line AGN. We attribute the weak broad Balmer emission to the broad-line regions hidden partially by optically-thick obscuring matter which also hides the optical and X-ray continuum emission from the accretion disc. Compton-thick obscuration, which would strongly suppress X-ray emission, could be due to a dense inter-stellar medium that is often present in galaxies at high redshifts. Alternatively, the same effect could be obtained from an inflated disc at the innermost radii in a supercritical accretion flow, when the disc is viewed at inclined angles.

Key words. Galaxies: high-redshifts - Galaxiers: active - quasars: general - X-rays: galaxies

1. Introduction

Both X-ray surveys and theoretical studies indicate that obscuration of active galactic nuclei (AGN) increases towards higher redshift, and the obscured AGN fraction at $z > 4$ could be as high as 80-90% (Gilli et al. 2022; Ni et al. 2020; Davies et al. 2019; Trebitsch et al. 2019; Vito et al. 2018; Liu et al. 2017). X-ray observations prove to be an useful tool in searching for obscured AGN, owing to the penetrating nature of X-rays (e.g. Hickox & Alexander 2018). The search for obscured quasars at high redshift is helped by the negative k-correction of an absorbed X-ray spectrum, unless the obscuration is heavily Compton-thick. In the absence of broad emission lines, optical-UV AGN signatures indicating a powerful ionising source, together with X-ray detection, would give a convincing case for obscured AGN. Despite the expected abundance of obscured AGN at high redshift, few examples showing both AGN narrow emission-line features and powerful X-ray emission have been found.

The "Subaru High-z Exploration of Low-Luminosity Quasars" (SHELLQs) project (Matsuoka et al. 2016) searches for quasars in the redshift range of $z > 5.6$, based on the Hyper Suprime-Cam (HSC, Miyazaki et al. 2018) Subaru Strategic

Program (SSP) wide-field imaging survey (Aihara et al. 2018). The majority of these quasars lie in the intermediate luminosity range between those discovered by earlier works based on shallower surveys (e.g. Fan et al. 2006; Willott et al. 2005; Jiang et al. 2015) and faint broad-line AGN including Little Red Dots (LRDs), recently found by James Webb Space Telescope (JWST) spectroscopy (e.g. Harikane et al. 2023; Übler et al. 2023; Greene et al. 2024; Matthee et al. 2024; Maiolino et al. 2024; Juodžbalis et al. 2024; Wang et al. 2024; Schindler et al. 2024; Furtak et al. 2024; Kocevski et al. 2024). The SHELLQs quasars in this luminosity range are quite rare, requiring a sensitive survey over the large area $\sim$ 1000 deg^2 of the Subaru HSC SSP to be discovered. The SHELLQs quasars include 18 faint objects with luminous narrow Lyα (Matsuoka et al. 2018a,b, 2019). They are characterised by their Lyα line widths and luminosities: FWHM $<$ 500 km s^{-1} [see the cumulative density function (CDF) of FWHM(Lyα) in Fig. 1] and L(Lyα) $> 1 \times 10^{43}$ erg s^{-1} (Matsuoka et al. 2018b). It has been known that Lyα emitters (LAEs) exceeding this luminosity are dominated by AGN (Konno et al. 2016; Sobral et al. 2018). Similar narrow-line quasar candidates have been discovered at lower redshifts (e.g. Alexandroff et al. 2013), but few were known at $z \sim 6$ (Willott et al. 2009; Kashikawa et al. 2015). Some of the SHELLQs narrow-line objects have L(Lyα) exceeding 10^{44} erg s^{-1}, more luminous than any known star-forming LAEs, whereas they show faint UV continuum emission, consistent with galaxy light with $M_{1450} \geq -22$. These objects can be considered as good obscured AGN candidates. Keck-MOSFIRE near-infrared spectroscopy of one of the narrow-line objects, J142331.71–001809.1, revealed narrow CIV doublet $\lambda\lambda$1548, 1550 with a rest-frame equivalent width, EW$\simeq$ 37Å (Onoue et al. 2021). Since the maximum EW of CIV expected in star forming galaxies is 10Å (Nakajima et al. 2018), this strongly suggests the presence of hard ionising photons from an AGN.

Here we describe X-ray observations of four of these narrow-line objects with the Chandra X-ray Observatory (Chandra hereafter), which resulted in no detection. Combined with results of recently acquired JWST rest-frame optical spectra of these objects which show broad Balmer lines (Matsuoka et al. 2025), we conclude that these objects may be higher-luminosity versions of the JWST-selected AGN, as they share similar properties. This paper is structure as follows: Sect. 2 describes the target selection, followed by the Chandra observations (Sect. 3) and the results (Sect. 4). Sect. 5 discusses implications of the results, including the JWST spectroscopy of the targets. We adopt the cosmological parameters $H_0 = 70$ km s^{-1} Mpc^{-1}, $\Omega_M = 0.3$, and $\Omega_\Lambda = 0.7$.

2. Target selection

2.1. Lyα properties

We selected Chandra targets from among the 18 SHELLQs narrow-line quasar candidates discovered as of Matsuoka et al. (2019). Fig. 2 show the M_{1450} - L(Lyα) diagram of SHELLQs quasars, divided into broad-line (FWHM $\geq$ 500 km s^{-1}) and narrow-line objects (Fig. 1). A loose correlation between the line and continuum luminosities can be seen. There are five objects that lie more than 2σ from the linear fit to M_{1450} against log L(Lyα) for the full SHELLQs sample[1]. The five outliers happen to have the largest Lyα luminosities among the narrow-line objects. The high EW of Lyα is consistent with a suppressed UV continuum in an obscured AGN. As shown in Fig. 2, they might be objects at the extreme end in luminosity of the population of luminous LAEs at $z \sim 6$ detected in the Subaru HSC survey (Shibuya et al. 2018), which could also contain AGN. We thus selected these five objects as possible obscured AGN candidates.

[1] If these five points are excluded, we find a steeper correlation between M_{1450} and log L(Lyα), and a scatter reduced by 30%

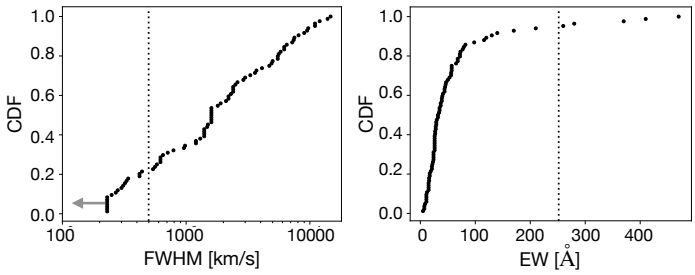

Fig. 1: Line widths (FWHM) and rest-frame equivalent width (EWs) of Lyα of SHELLQs quasars. Left panel: CDF of FWHM(Lyα) in units of km s^{-1}. Seven objects show unresolved lines that have an upper limit on FWHM of 230 km s^{-1}. Dotted line indicates the dividing line at 500 km s^{-1} below which narrow-line objects are defined. Right panel: CDF of EW(Lyα). Dotted line indicates 250 Å, above which five outliers in Fig. 2, including the four Chandra targets are found.

Due to the limited observing time awarded for this program, one of the candidates, J114658.96–000537.6 (z = 6.30) was left out and the other four objects were observed with Chandra. Table 1 gives rest-frame UV properties of the four targets. We refer these objects as G01, G02, G03 and G04 hereafter, as given in the companion paper on JWST results by Matsuoka et al. (2025). They have Lyα emission with luminosities exceeding 10^{44} erg s^{-1} and EW ranging between 280Å and 470Å in the rest frame (Table 1, Fig. 1).

The mean line profile of Lyα of the four objects, obtained from the Subaru-FOCAS (Matsuoka et al. 2019), which was constructed after normalising the spectra by the line peak, is shown in Fig. 3. The line profile of this composite shows a weak red-wing (the line profile bluewards is absorbed by the Lyα forest). This wing component has a FWHM of $\sim$ 2000 km s^{-1} (detailed fits of the line profiles of individual objects are presented in Matsuoka et al. (2025)). Although this broad component could be attributed to the BLR of AGN, other causes such as an outflow and resonant scattering (e.g. Osterbrock 1962) might be in play. We note that there is no clear sign of N Vλ1240Å with a P Cygni profile, seen in the composite spectrum of all SHELLQs narrow-line objects presented in Matsuoka et al. (2019).

The observed UV continuum luminosities of these objects are all fainter than $M_{1450} = -22$, and thus can be attributed to galaxy emission alone, as the number density of galaxies is about three orders of magnitude above that of unobscured quasars at $z \sim 6$, suggested by their respective luminosity functions (Matsuoka et al. 2018c).

2.2. X-ray detection experiment

The observation of the Lyα emission line was the only clue we had before the X-ray observations for how powerful possible AGN in these sources might be. Its luminosity can be a rough guide of AGN luminosity: although statistically there is a positive correlation between the luminosities of Lyα and X-ray in AGN (Calhau et al. 2020), the scatter of the correlation and sparse sampling of the large Lyα luminosity range mean that

Table 1: Chandra targets

Name	Object	z	FWHM km s^{-1}	EW Å	log L(Lyα) [erg s^{-1}]	M_{1450} mag
G01	J142331.71–001809.1	6.127	< 230	370	44.30	−21.88
G02	J084456.62+022640.5	6.397	< 230	280	44.05	−21.57
G03	J093543.32–011033.3	6.075	< 230	410	44.12	−21.97
G04	J125437.08–001410.7	6.130	310	470	44.03	−20.91

Notes. Short target names, G01..G04, used in this work are identical to those used in Matsuoka et al. (2025). Object names follow the Subaru HSC survey naming convention and convey right ascension and declination in J2000 coordinates for each source. The redshifts shown here are updated values, obtained from the JWST-NIRSpec spectra (Matsuoka et al. 2025). FWHM is the full width at half maximum of Lyα as measured, without correction for absorption of the intergalactic medium. EW is the rest-frame equivalent width of Lyα. M_{1450} is absolute magnitude at 1450 Å.

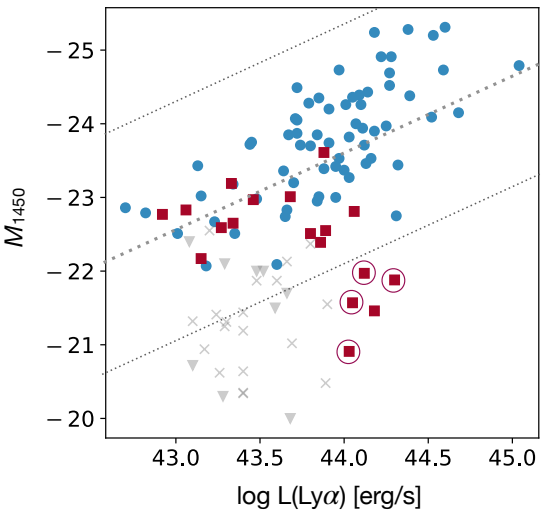

Fig. 2: UV absolute magnitude M_{1450} as a function of Lyα luminosity of SHELLQs quasars. Broad-line (FWHM(Lyα)≥ 500 km s^{-1}) and narrow-line (FWHM(Lyα)< 500 km s^{-1}) objects are plotted with blue circles and red squares, respectively. The four Chandra targets are circled in red. Dashed line indicates the best linear fit to both broad- and narrow-line objects. The two dotted lines show the 95% compatible intervals. Data for LAEs at $z \sim 6$ detected in the Subaru HSC survey from Shibuya et al. (2018) are also plotted in grey for comparison. Crosses are LAEs for which UV continuum emission was detected while triangles are those for which only upper limits of UV emission were obtained.

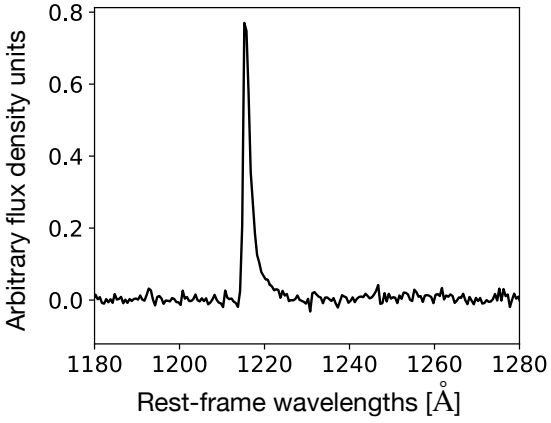

Fig. 3: Mean Lyα profile of the four Chandra targets.

L(Lyα) is not a reliable L_X predictor for an individual object. We therefore took an alternative route and predicted their L_X based on their surface density, as described below, and designed the Chandra observations as a detection experiment in which only a few source counts are expected.

Five obscured AGN candidates which are outliers of the M_{1450}-L(Lyα) correlation (Sect. 2.1) were found in the survey area of 900 deg^2. Suppose obscured AGN outnumber unobscured AGN by a factor of β, and the obscuration-corrected luminosity function of obscured AGN has the same shape as that of the known quasars at $z \sim 6$ of Matsuoka et al. (2018c). We assume β to be in the range of 1 to 10, which is equivalent to an AGN obscured fraction $f_{\rm obsc} = 0.5$-0.91. The lower bound corresponds to the limit of obscuration caused only by circumnuclear hot dust found in quasars at $z \sim 2$ (Lusso et al. 2013). The higher bound matches the value $f_{\rm obsc} > 0.82$ derived from the proximity zone analysis for $z > 7$ quasars by Davies et al. (2019). Given this hypothetical luminosity function, you can obtain a luminosity that yields the observed surface density. For the two extreme values of β, the UV absolute magnitudes to yield five objects per 900 deg^2 are $M_{1450} \simeq -25.7$ ($\beta = 1$) and $M_{1450} \simeq -27.7$ ($\beta = 10$). Using the known luminosity-dependent UV to X-ray relation (Vito et al. 2019), the corresponding rest-frame 2-10 keV luminosities, L_X, are 4×10^{44} erg s^{-1} ($\beta = 1$) and 1.3×10^{45} erg s^{-1}($\beta = 10$). If the targets emit at luminosity in the above range and have a power-law spectrum of photon index $\Gamma = 2$, source counts expected in the 1-5 keV band for a 60 ks Chandra ACIS-S observation range from five to 15 counts for $z = 6.1$, even if the equivalent hydrogen absorbing column density of obscuration is as large as $N_{\rm H} \sim 10^{23}$ cm^{-2}.

3. Observations

Chandra observations of the four SHELLQs narrow-line objects were carried out during the Cycle 23. Each target was observed with three or four exposures to achieve an integrated exposure time of approximately 60 ks, as shown in Table 2. All the targets were placed on the ACIS-S3 chip, operating in the VFAINT mode. The Galactic absorption for each target ranges from $N_{\rm H} = 1.4 \times 10^{20}$ cm^{-2} to $N_{\rm H} = 3.9 \times 10^{20}$ cm^{-2}, according to the HI4PI map (HI4PI collaboration, 2016). The Chandra ACIS detector of the current effective area is not sensitive to this amount of small Galactic absorption. Data reduction was performed in the standard manner using CIAO 4.15 (Fruscione et al. 2006).

Table 2: Chandra observation log

Name	ObsID	Date	Exposure
G01	25370	2021-12-14	19.82
	25905	2023-05-07	27.11
	26237	2021-12-15	9.82
G02	25371	2023-01-26	14.74
	25894	2022-02-03	13.90
	26300	2022-02-04	14.76
	27675	2023-01-27	13.20
G03	25373	2023-02-06	15.86
	25740	2022-10-10	11.95
	27478	2022-10-12	15.68
	27699	2023-02-06	13.71
G04	25372	2022-04-06	13.77
	25862	2023-04-10	14.88
	26379	2022-04-06	16.85
	27797	2023-04-10	14.88

Notes. Exposure time is in units of 10^3 seconds. All the observations were carried out with the ACIS-S3 operating in VFAINT mode.

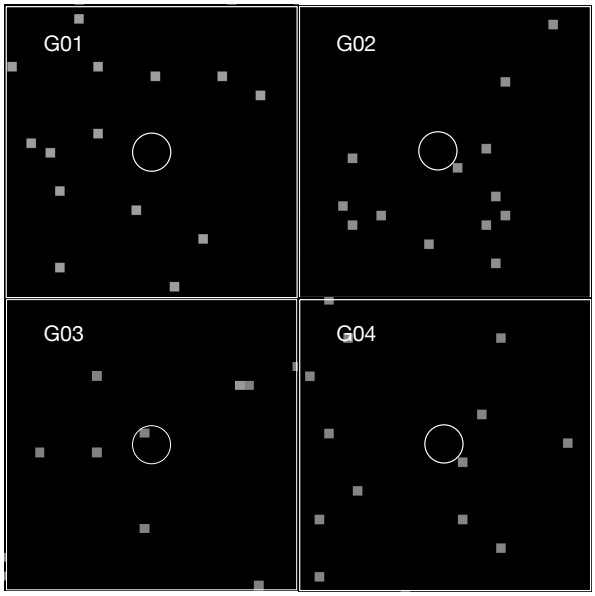

Fig. 4: Chandra 1-5 keV images of the four narrow-line SHELLQs quasars. Each panel is a 15″×15″ field of view centred on the target. The image orientation is North up, East to the left. The circle indicates the optical position with a 1 arcsec radius.

4. Results

X-ray images of each target were constructed by stacking the repeat exposures. The total exposure times are and 56.7 ks for G01, 56.5 ks for G02, 57.0 ks for G03, and 60.0 ks for G04, respectively. We examined those images in the 1-5 keV band, where the signal to noise ratio is expected to be optimal owing to low instrumental background. None of the targets were detected (Fig. 4). With the point spread function (PSF) of the ACIS-S, 60% of counts from a point source are expected to fall within a 1-pixel (= 0.49″) radius (MARX document 5.2.2). No counts were observed within a 1-pixel radius from any of the four target positions. The background counts in the 1-5 keV band are 0.013-0.015 cts pixel^{-1} for these observations. Therefore no background count is expected (the probability of observing one or more background counts in the area is 4%), as observed. Detection of no counts sets the 95% upper limit to be 3 counts in each aperture, using a Bayesian formulation for a Poisson distribution of counts (Kraft et al. 1991). Assuming that each source has a photon-index $\Gamma = 2$ (e.g. Huang et al. 2020) and absorbing column $N_{\rm H} < 10^{23}$ cm^{-2}, the corresponding rest-frame 2-10 keV luminosity at the median redshift of the four targets, $z = 6.13$, is 2×10^{44} erg s^{-1}, which we adopt as the upper limit for each object for the discussion below.

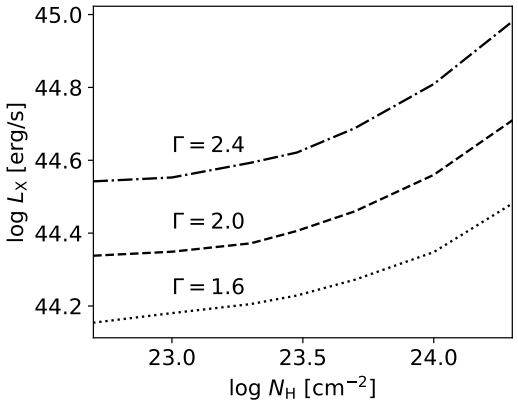

Fig. 5: Upper limit of intrinsic $L_{\rm X}$ corresponding to 3 counts (the 95% upper limit obtained from a 60 ks exposure) for different assumed spectral slope Γ. $L_{\rm X}$ is the unabsorbed, rest-frame 2-10 keV luminosity. Examples for three values of photon index Γ = 1.6 (dotted line), 2.0 (dashed line) or 2.4 (dot-dashed line) as a function of $N_{\rm H}$ are shown.

We note that one count was registered at 0.8 arcsec (within a 2-pixel radius) from the target position in the G03 image. Given the PSF, the probability of detecting one source count in the second radial pixel but none in the first is 10%. Given the background level, observing one background count within the same area has a probability of 12%, assuming a Poisson process. Since the Bayes factor is around unity, no preference is given whether it is a source or background count. Even if it is a source count, the one count does not constitutes a detection, but gives an increased upper limit of 4.7 counts for G03, corresponding to 3×10^{44} erg s^{-1}.

If the spectral slope differs from $\Gamma = 2$ and the absorbing column $N_{\rm H}$ is larger than 10^{23} cm^{-2}, the upper limit of intrinsic (unabsorbed) $L_{\rm X}$ will be different. Fig. 5 shows the 95% upper limits on $L_{\rm X}$ corresponding to 3 counts, when photon index is Γ = 1.6, 2.0 or 2.4, as a function of absorbing column density, $N_{\rm H}$.

We have four targets with approximately equal exposure times. If our four targets have similar X-ray luminosities, as in the case for Lyα — the mean is $10^{44.1}$ erg s^{-1} and the standard deviation in the log is only 0.1 —, their average X-ray luminosity can be constrained by stacking all the observations. When a 2-pixel radius around the target position is adopted and the one count registered in all the observations is considered, a 95% upper limit of 1.0 count per object is obtained following the formulations of Weisskopf et al. (2007). For $\Gamma = 2$, this corresponds to $L_{\rm X} = 0.8 \times 10^{44}$ erg s^{-1}, which we consider as the upper limit of the average $L_{\rm X}$ from stacking.

5. Discussion

The fact that we did not detect X-rays from these sources suggests the possibility that these objects are not AGN, and star formation is responsible for the luminous Lyα. If that is the case, they would have low metallicity of $Z < 0.01Z_{\odot}$ and a young age (less than 10^6 yr) of intense star formation (Hashimoto et al. 2017), since normal star forming galaxies cannot produce EW(Lyα)> 240Å (Malhotra & Rhoads 2002). However, recently acquired JWST spectra of the Chandra targets favour presence of AGN for all four objects (Matsuoka et al. 2025). We briefly discuss the implications of the JWST results and, if AGN exist, how their X-ray emission remains below the detection limit.

5.1. Selection bias

One of the selection criteria of quasar candidates from the Subaru HSC imaging data is that a candidate source to be point-like[2] (Matsuoka et al. 2018b), which optimises the original purpose of selecting unobscured quasars in which AGN emission dominates the rest-frame UV light. On the other hand, the HSC image of an obscured AGN is primarily due to emission from the host galaxy, and thus could be extended. This would mean that some obscured AGN candidates would be missed, and the true number of obscured quasars could be larger than actually discovered under the adopted criteria. In Sect. 2.2, we made the crude estimate of the typical $L_{\rm X}$ of our Chandra targets using the targets' surface density and an assumed luminosity function as a function of the ratio of obscured to unobscured AGN (β = 1-10). The possible underestimate of obscured quasars mentioned above would then lower the typical luminosity of the obscured quasars that can be selected in the Subaru HSC survey. This could be consistent with no detection of the Chandra targets, but a question is the extent to which we missed obscured quasars.

The upper limit value of the average luminosity for our Chandra targets obtained above (corresponding to $M_{1450} \sim -24$) gives a number of obscured quasars five times larger for $\beta = 1$ or ~ 100 times larger for $\beta = 10$ than those selected for our Chandra observations (that is, five, including the one left out), using the shape of the luminosity function of Matsuoka et al. (2018c). Given the negative slope of the luminosity function, these are lower limits of the obscured quasar number. While missing a factor of four more obscured quasars by applying the point source criterion, as found for $\beta = 1$, might just be possible, missing by ~ 100 times more objects ($\beta = 10$) seems unlikely. On the other hand, a large value of β, close to $\beta = 10$, is generally favoured, as argued in Sect. 1. This means that the selection bias against obscured quasars is insufficient by a large margin to explain the null X-ray detection.

5.2. Implications from JWST spectroscopy

5.2.1. Broad Balmer emission

Rest-frame optical spectra of the four Chandra targets have been obtained using JWST-NIRSpec during Cycle-2 (Program ID 3417). All four spectra show weak broad Balmer emission with FWHM~2000 km s^{-1} at the base of narrow lines, reminiscent of those of JWST-selected AGN. Detailed results are presented in Matsuoka et al. (2025). Here we present an extract of emission-line properties relevant to this work in Table 3. Extinction was derived from Balmer decrements of narrow and broad components separately, and luminosities have been corrected for the corresponding extinctions. As broad emission is seen both in Hα and Hβ, they resemble optical spectra of Seyfert 1.8 (Osterbrock 1977, although J1254–0014 with stronger broad emission than the others barely qualifies as Seyfert 1.5 when the criterion of Winkler (1992) is applied). A straightforward interpretation of the broad Balmer emission is that it originates from the BLRs of AGN.

[2] Extended sources are also selected as high-redshift quasar cadidates, but they are given lower priority for spectroscopic follow-up.

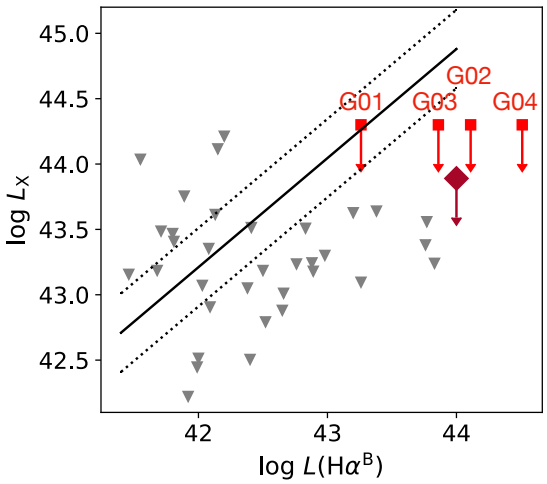

Fig. 6: $L_{\rm X}$ against L(Hα) diagram. The four Chandra targets are indicated by red squares and $L_{\rm X}$ values are 95% upper limits. The diamond symbol shows the result of stacking the four. Grey triangles indicate LRDs at z = 3-7 from Yue et al. (2024a), when $N_{\rm H} = 10^{22}$ cm^{-2} is assumed. The $L_{\rm X}$ values are also 95% upper limits, adjusted from the original 3σ upper limits. The black solid line shows the $L_{\rm X}$-L(Hα) relation for broad-line AGN of Jin et al. (2012). Dotted lines indicate ±0.3 dex interval of the relation, corresponding to the data scatter. These lines are drawn over the L(Hα) range covered by the Jin et al. (2012) sample.

In low-redshift unobscured AGN, broad-line Hα luminosity correlates with $L_{\rm X}$ and AGN bolometric luminosity, $L_{\rm bol}$ (Jin et al. 2012; Stern & Laor 2012b; Greene & Ho 2005; Kaspi et al. 2000). Fig. 6 plots extinction-corrected broad Hα luminosity and $L_{\rm X}$ upper limit of the Chandra targets, with the $L_{\rm X}$ - L(Hα) relation derived for broad-line AGN at low redshift(Jin et al. 2012) superposed. For a comparison, the LRDs at z = 3-7 (Yue et al. 2024a), none of which were detected in X-ray, are also plotted. While the limits for G01, which has the weakest broad Balmer emission among the four, still remain consistent with ordinary AGN, the limits for the other three indicate that they are deficit in X-ray, although the constraints are not as tight as some of the LRDs in the deep X-ray survey fields.

5.2.2. Obscured BLRs and continuum source

The Balmer line profiles with a strong narrow core shows that the broad emission in these objects is systematically weaker than those of typical broad-line quasars. In addition to small to moderate extinction for the NLRs, the visibility of broad Hβ means that extinction for the BLRs cannot be large and is insufficient to suppress the broad Hα as observed (Table 3). This implies either that the BLR emission is intrinsically weak, or only part of the BLRs is visible. The former could occur for a low Eddington ratio $\lambda_{\rm Edd} < 10^{-2}$ (e.g. Elitzur & Ho 2009; Kang et al.

Table 3: Results from JWST-NIRSpec observations.

Name	A_V^N	A_V^B	$L(H\alpha^N)$	$L(H\alpha^B)$	$L([O\,III])$	L_{5100}^{obs}	L_{bol}	$EW(H\alpha^B)$
G01	0.10 ± 0.04	2.15 ± 0.56	43.29 ± 0.01	43.43 ± 0.18	43.64 ± 0.02	44.84 ± 0.25	46.42 ± 0.02	580 ± 160
G02	0.43 ± 0.10	0.98 ± 0.07	43.35 ± 0.03	44.04 ± 0.02	43.84 ± 0.04	44.92 ± 0.03	46.61 ± 0.04	938 ± 18
G03	0.94 ± 0.09	1.27 ± 0.13	43.58 ± 0.03	43.81 ± 0.04	43.90 ± 0.04	44.84 ± 0.06	46.68 ± 0.04	775 ± 31
G04	1.75 ± 0.08	1.88 ± 0.07	43.63 ± 0.03	44.36 ± 0.02	44.00 ± 0.04	45.18 ± 0.03	46.78 ± 0.04	1356 ± 26

Notes. Extract from JWST-NIRSpec spectroscopy results from Matsuoka et al. (2025). Extinction, A_V, of NLRs (N) and BLRs (B), derived from Balmer decrement. Luminosity of narrow and broad Hα emission, [O III]λ5007 emission, and continuum at 5100 Å. $L(H\alpha^N)$ and $L([O\,III])$ have been corrected for the NLR extinction, while $L(H\alpha^B)$ and L_{5100}^{obs} corrected for the BLR extinction. L_{bol} is bolometric luminosity estimated from $L([O\,III])$. All luminosities are in logarithmic values and in units of erg s^{-1}. Rest-frame EW of broad Hα in units of Å.

2024). However, in this case, it would be accompanied by a hard SED, that is, X-ray emission that is strong relative to UV (Ferland et al. 2020). Since this does not match the observations, this hypothesis seems unlikely. Moreover, given the large bolometric luminosities (see Fig. 8) their inferred black hole masses would be close to or in excess of $10^{10}\,M_\odot$, which is unlikely at $z \sim 6$ (e.g. Wu et al. 2015). More probable is the latter model, in which the bulk of the BLRs is totally hidden. If an optically-thick obscuring torus is present, a part of the BLRs can be hidden at intermediate viewing angles, and strength of broad-line emission depends on the visiblility of the BLR clouds.

We next make a crude estimate of the total broad Hα luminosity and its visible proportion. For broad-line AGN at low redshift, Jin et al. (2012) found that the narrow component of Hα emission[3] comprises, on average, $10 \pm 8\%$ of the total flux. Assuming the same composition, a broad component luminosity, $L'(H\alpha^B)$, that includes the hidden portion, can be estimated, using the observed narrow Hα luminosity (Table 4). Comparing this estimate with the observed $L(H\alpha^B)$ gives the fraction of the BLRs which is visible, f_{BLR}, ranging from 9% to 52% (Table 4).

The JWST spectra also show faint optical continuum emission. Given a broad Hα luminosity, the empirical relation of Greene & Ho (2005) gives a 5100 Å luminosity, $L_{5100}^{H\alpha}$, with uncertainty $\simeq 0.2$ dex. The observed luminosity, L_{5100}^{obs} (corrected for A_V^B), is expected to match that obtained from a broad Hα luminosity, $L_{5100}^{H\alpha}$, or larger as there is a contribution from host galaxy light in the observed continuum. However, L_{5100}^{obs} values for the Chandra targets are, on the contrary, lower than the expected values based on this argument[4], except for G01 with a large uncertainty (Fig 7). Since our targets have $L(H\alpha)$ more luminous than the Greene & Ho (2005) sample of low-redshift ($z < 0.35$) SDSS broad-line AGN with $L(H\alpha)$ only up to 10^{44} erg s^{-1}, we tested the extrapolation of the relation against five luminous, unobscured quasars with $L(H\alpha) > 10^{44}$ erg s^{-1} at z = 6-7, observed with JWST (Marshall et al. 2023; Loiacono et al. 2024; Bosman et al. 2024; Yue et al. 2024b; Marshall et al. 2025). These high-redshift quasars instead all show positive values of $\log (L_{5100}^{obs}/L_{5100}^{H\alpha}) \approx 0.1$-0.4, while any host galaxy contribution in these quasars should be negligible. The updated reference value for luminous, high-redshift unobscured quasars with those data is indicated in Fig. 7 with a predicted 68% scatter interval. Therefore it is likely that the Chandra targets show continuum deficit given the $L(H\alpha^B)$, represented by negative values of $\log (L_{5100}^{obs}/L_{5100}^{H\alpha})$. This implies that the AGN continuum in the Chadra targets is suppressed more than the visible BLR emisison. The observed large EWs of broad Hα (Table 3) are in accord with this conclusion. These EWs from 580 Å to 1356 Å are larger than in low-redshift SDSS quasars that typically have EW $\sim$ 200 Å, and similar to values for JWST-selected AGN (Maiolino et al. 2025). Negative values of $\log (L_{5100}^{obs}/L_{5100}^{H\alpha})$ and large EWs of broad Hα, as discussed above, also hold for the other five SHELLQs narrow-line objects with broad Hα detection of Matsuoka et al. (2025). If part of the BLRs is hidden, as we argued, the continuum source in our objects should be totally hidden, too, due to its inner location, and the observed continuum could be dominated by host galaxy light, apart from possible scattered light (related discussion can be found in Matsuoka et al. (2025)).

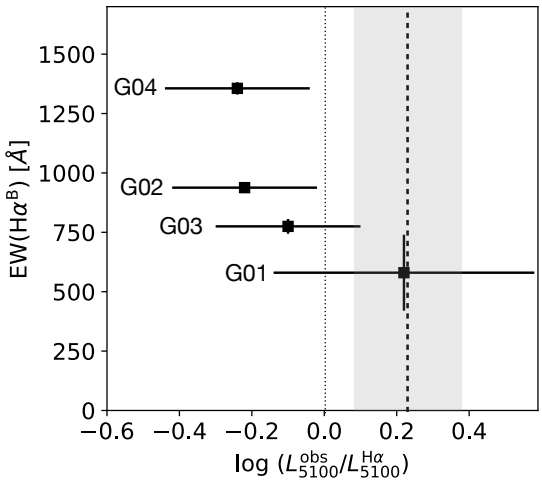

Fig. 7: Rest-frame EW of broad Hα in units of Å as a function of optical continuum deficit at 5100 Å given the broad Hα luminosity, represented by $\log (L_{5100}^{obs}/L_{5100}^{H\alpha})$. The dotted line indicates the empirical L_{5100}-$L(H\alpha^B)$ relation by Greene & Ho (2005) for SDSS AGN at $z < 0.35$. The dashed line and the shaded area show $\log (L_{5100}^{obs}/L_{5100}^{H\alpha}) = 0.22$, updated by data for luminous quasars at z = 6-7 and the 68% interval of posterior predictives, respectively.

5.2.3. X-ray quietness

Assuming the hypothesis that the BLRs in these sources are partially hidden, the observed broad Hα luminosity depends on the fraction of the BLRs directly visible and the true luminosity should be larger than the observed value. Thus we re-evaluate the broad Hα-based L_X of AGN, given our knowledge of low-

[3] Jin et al. (2012) modelled Balmer lines with three components. As their narrow component matches the profile of [O III], it corresponds to our narrow component, as defined in Matsuoka et al. (2025).

[4] We note that the luminosity of broad Hα used here is the observed one (Table 3), not $L'(H\alpha)$ discussed above.

Table 4: Correction for hidden BLRs and L_X predictions

Name	$L'(H\alpha^B)$ (1)	f_{BLR} (2)	$L_X'^{H\alpha^B}$ (3)	L_X^{OIII} (4)
G01	44.24	0.15	45.07 (45.00)	44.96
G02	44.30	0.54	45.12 (45.03)	45.16
G03	44.53	0.19	45.31 (45.16)	45.22
G04	44.58	0.59	45.35 (45.18)	45.32

Notes. (1) Broad Hα luminosity, corrected for the fraction of the BLR that is hidden (see text in Sect. 5.2.3). (2) Visible fraction of the BLRs. (3) 2-10 keV luminosity inferred from the L_X-L(Hα) relation of Jin et al. (2012) and $L'(H\alpha^B)$ in column (1). Those in parentheses are values corrected for a possible over-estimate that originates from an extrapolation of the relation (see text in Sect. 5.2.3). (4) 2-10 keV luminosity, estimated from the typical absorption-corrected X-ray to extinction-corrected [OIII]λ5007 ratio of log (L_X/L([OIII]) = 1.32. Luminosities are logarithmic values in units of erg s^{-1}. Uncertainty of these luminosities comes from the scatter of the relations adopted, about 0.3 dex.

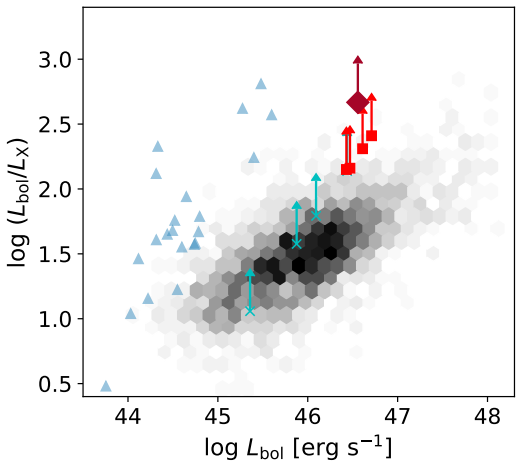

Fig. 8: X-ray to bolometric luminosity ratio (L_{bol}/L_X) against L_{bol}. The four Chandra targets are indicated by red squares. The diamond symbol shows the result of stacking the four. Cyan crosses are those for the individual objects where L_{bol} was estimated from broad Hα (see Table 3 and Fig. 6). Blue triangles indicate JWST-selected AGN from Maiolino et al. (2025), where L_{bol}/L_X values are all lower limits, as X-ray emission was detected from none of these sources. Data for broad-line quasars (Lusso et al. 2020) are shown in grey-scale two-dimensional histogram.

redshift broad-line AGN. With the corrected Hα luminosities, L'(Hα), the L_X-L(Hα) relation (Jin et al. 2012) predicts X-ray luminosities (L_X') exceeding 10^{45} erg s^{-1} for all the Chandra targets (Table 4). We note that, as those L'(Hα) are above the luminosity range ($\leq 10^{44}$ erg s^{-1} in Hα) where the L_X-L(Hα) relation was derived, an extrapolation of the relation may overestimate L_X, since L_X/L_{UV} decreases towards higher luminosities. With the known L_X-L_{UV} relation for quasars (e.g. Vito et al. 2019; Lusso & Risaliti 2016, see also Fig. 8), we found the possible over-estimate in L_X' to be 0.07 dex to 0.17 dex. Even taking this into account, the predicted L_X are still found to be 10^{45} erg s^{-1} or larger (Table 4).

Similar L_X values are also expected from the observed [OIII]λ5007 luminosity, which is considered to be a reliable indicator of isotropic AGN power (e.g. Kauffmann et al. 2003; Shen et al. 2011; Rakshit et al. 2020), especially when the BLRs are obscured as in Type 2 AGN. In particular, [OIII] is correlated with absorption-corrected L_X. The luminosity ratio of 2-10 keV X-ray to [OIII] measured for low-redshift AGN is log (L_X/L([OIII])$\approx$ 1.9 (Mulchaey et al. 1994; Heckman et al. 2005; Trouille & Barger 2010; Georgantopoulos & Akylas 2010; Jin et al. 2012; Stern & Laor 2012a; Berney et al. 2015; Malkan et al. 2017). The scatter of this ratio from various paper ranges from 0.3 dex to 0.5 dex. These values are derived, however, with [OIII] luminosities with no extinction correction. Jin et al. (2012) obtained one of the typical values, 1.88, which reduces to 1.32 when extinction correction from the mean Balmer decrement (Hα/Hβ = 5.0) for their broad-line AGN sample is applied. Using this value, our Chandra targets are expected to have L_X = (1-2) $\times$ 10^{45} erg s^{-1}(Table 4).

The agreement between the predicted L_X (and hence bolometric luminosities, L_{bol}) by two independent estimators, L([OIII]) and corrected $L'(H\alpha^B)$, gives some credence to the assumption of partially hidden BLRs. Fig. 8 shows the bolometric to X-ray luminosity ratio, L_{bol}/L_X (or X-ray bolometric correction), against L_{bol} for the Chandra targets on the diagram, similar to Fig. 2 of Maiolino et al. (2025). The data points for the Chandra targets using L_{bol} estimated from L([OIII]) (Matsuoka et al. 2025) are plotted, together with lower limits for JWST-selected AGN at z = 4-7 (Maiolino et al. 2025) and the two-dimensional histogram of broad-line quasars at z = 0.01-7 (mostly $z \leq 3$) studied by Lusso et al. (2020)[5]. When L_{bol} is estimated from the observed broad Hα luminosity (which might be underestimated as argued above), the individual data points shift to those of cyan crosses.

The luminosities of strong narrow lines are similar between the four objects: the logarithmic means and standard deviations of the luminosities of narrow Hα and [OIII] in units of erg s^{-1} are 43.59 (0.19) and 43.83 (0.10). The small dispersion of these line luminosities leads to similar predicted L_X (Table 4) and L_{bol} (Fig. 8, Table 3). Incidentally, these values agree with the estimates in Sect. 2.2 based on the surface density with a large $\beta \sim 10$.

The X-ray upper limits obtained from Chandra observations are nearly one order of magnitude (1.5 dex for the stack) below the expected L_X argued above (see also Fig. 8). We discuss possible causes of the X-ray quietness of these objects below.

5.3. Possible explanations of X-ray quietness

The X-ray quietness of these objects can be due either to intrinsically weak X-ray emission or to heavy obscuration. The former possibility is linked to a steep UV to X-ray SED in a super-Eddington accretion flow, as discussed for the JWST-selected AGN (Inayoshi et al. 2024; Maiolino et al. 2025). Here we discuss the latter. The Chandra bandpass we observed (1-5 keV)

[5] The bolometric luminosities of the Chandra targets were taken from Table 8 of Matsuoka et al. (2025), which are estimated from [OIII]λ5007 luminosities. For those based on broad Hα luminosities, the extinction-corrected broad Hα luminosities in Table 3 were used. The AGN continuum luminosity at 5100 Å, $L_{5100}^{H\alpha}$, was first estimated, using the empirical relation (Greene & Ho 2005), and then converted to L_{bol} with the bolometric correction of 7.79 (Krawczyk et al. 2013). For those broad-line quasars, L_{bol} was derived from monochromatic luminosity at 2500 Å given in Lusso et al. (2020) with the bolometric correction of 2.75 (Krawczyk et al. 2013) while L_X was derived from the 2 keV luminosity assuming Γ = 2 as the spectral slope in the 2-10 keV band. The values of L_X for JWST-selected AGN have been adjusted by matching the same assumed spectral slope (Γ = 1.7 was assumed in Maiolino et al. (2025)).

corresponds to 7-35 keV in the rest frame. Suppressing this hard X-ray emission requires a significantly Compton-thick absorbing column of $N_{\rm H}>> 10^{24}$ cm^{-2}.

5.3.1. Compton-thick absorption by interstellar medium

In the hypothesis of partially hidden BLRs argued above, the X-ray source is located behind the same obscuring matter at intermediate viewing angles. Although this picture is similar to the unification scheme of Seyfert galaxies with a pc-scale torus (Antonucci & Miller 1985), nuclear obscuration may take a different form at high redshifts, as argued by Gilli et al. (2022). With the increased gas content in galaxies (e.g. Scoville et al. 2017), a galaxy-wide interstellar medium (ISM) is capable of making up a Compton-thick absorbing column over the bulk of solid angles. In fact, ALMA high-resolution maps of high-J transition CO lines of a quasar at $z = 6$ showed that warm molecular gas extends to 100-pc scales, for which a column density of $N_{\rm H}\simeq 10^{25}$ cm^{-2} is inferred (Tadaki et al. 2025). Given the small host galaxy size of the order of 1 kpc (Ding et al. 2023; Onoue et al. 2024, Ding et al. in prep.), this dense gas occupies a significant portion of the host galaxy. Even though the geometry is not yet clear, this form of Compton-thick gas can completely suppress X-ray emission in the Chandra targets, as well as the optical emission from inner radii.

Such extended obscuring matter has a thermal structure that is likely to deviate from that in the typical hot dust seen in low-redshift AGN (Barvainis 1987). This may, in part, be similar to an extended dusty region, proposed to explain the lack of a near-infrared bump in the rest frame in LRDs (Li et al. 2025). Photometric observation of the rest-frame near-infrared band for these SHELLQs narrow-line objects can probe the nature of the obscuring matter.

5.3.2. Obscuration with a supercritical accretion flow

If the idea of partially hidden BLRs is discounted and only mild obscuration, as implied from the values of extinction measured from the Balmer decrement (Table 3), is present for the optical emission region in these objects, then a distinct Compton-thick obscuration that solely affects the X-ray source is required. We consider a supercritical accretion flow as a possible mechanism of strong X-ray attenuation, when combined with an orientation effect, as discussed below.

In the disc accretion mode, as opposed to spherical accretion, matter falls along the disc plane while radiation can escape in the polar direction, enabling a supercritical accretion flow while emitting at super-Eddington luminosity (e.g. Ohsuga et al. 2005). A number of key features of such an accretion flow are described in the slim disc prescription by Abramowicz et al. (1988). One of the relevant features in our argument is an optically thick funnel created by the innermost part of the disc, which is inflated by strong radiation pressure. It collimates the disc radiation, making it anisotropic (Ohsuga et al. 2005; Ohsuga & Mineshige 2007; Takahashi & Ohsuga 2015; Sądowski et al. 2015; Jiang et al. 2019). In AGN, the disc radiation is in the UV range and an external mechanism is needed to produce X-rays. Kawashima et al. (2009, 2012) proposed that the radiation-pressure driven disc winds in a supercritical accretion flow can act as a Comptonising corona that produces X-rays (see also Jiang et al. 2019). The dynamical nature makes this wind-fed corona somewhat cooler and more optically thick than the conventional corona (e.g. Haardt & Maraschi 1991) above the standard thin disc in low-redshift AGN (Kawanaka & Mineshige 2021; Inayoshi et al. 2024). In this case, the X-ray emission is also anisotropic. We refer to Kawashima et al. (2012); Kitaki et al. (2017); Ogawa et al. (2021) for details of the viewing-angle dependence of X-ray luminosity and spectral shape.

Viewing such a system face-on, the whole X-ray emitting region, including the high-temperature (a few 10^8 K) part, deep down the funnel, is visible. Ultra-luminous X-ray sources (ULXs) are considered to fit in this situation (Kawashima et al. 2009; Kitaki et al. 2017; King 2024), and their AGN couterparts perhaps correspond to the most luminous, unobscured quasars. In quasars, however, disc emission moves to the UV range and the Compton-scattered emission dominates the X-ray range, unlike a stellar-mass black hole that emits X-ray disc emission. Given the cooler wind-fed corona, the X-ray spectra steepen above $\sim$ 10 keV, below which they can be as hard as low-redshift AGN that show Γ = 1.9-2.0, on average (e.g. Vignali et al. 2003; Steffen et al. 2006; Just et al. 2007; Lusso & Risaliti 2016; Nanni et al. 2017; Huang et al. 2020). Since XMM-Newton or Chandra bandpass mainly covers rest-frame energies higher than 10 keV in $z \geq 6$ quasars, a single power-law fit would yield a steeper slope, as observed in the most luminous quasars at $z \sim 6$ ($\Gamma \simeq 2.2$ and $\Gamma \sim 2.4$ respectively in Vito et al. 2019; Zappacosta et al. 2023). The fact that the spectral steepening is only found for high-redshift quasars could therefore be a combination of the rest-frame bandpass effect and a selection effect that spectral slope measurements are possible only for the most luminous quasars given the limited sensitivity. Due to the collimation, the X-ray luminosities of those most luminous quasars are likely boosted.

On the other hand, when the system is viewed at some inclined angle, the flux boosting effect disappears and the innermost part of the funnel, where hard X-rays are produced, is blocked from our direct view by the inflated inner disc which is optically thick. Any X-ray emission that is still visible is therefore much weaker and has a softer spectrum than that seen in the face-on case (Kitaki et al. 2017; Ogawa et al. 2021). Those luminous quasars at $z \sim 6$, such as those in the HYPERION sample (Zappacosta et al. 2023, see also Vito et al. (2019)) emit at $L_{\rm X} \sim 2 \times 10^{45}$ erg s^{-1} on average. If they are the face-on version of AGN with a supercritical accretion argued above, the same nuclei viewed at an intermediate angle would have an observed luminosity of a few times 10^{43}erg s^{-1}(for example, the rest-frame 20 keV emission when viewed at 40° would be $\sim$2 orders of magnitude fainter than when viewed face-on). As this expected $L_{\rm X}$ fits the Chandra upper limit, the SHELLQs narrow-line objects could contain nuclei similar to the HYPERION quasars but viewed at intermediate angles. Thus the inherent anisotropy of X-ray radiation at the innermost radii of a supercritical accretion flow offers an alternative explanation of the X-ray quietness of the Chandra targets.

6. Summary

We selected obscured AGN candidates at $z \sim 6$ from the SHELLQs sample for X-ray observations with Chandra, on account of thier luminous Lyα and faint UV continuum. We did not detect X-rays; this, together with subsequent detection of weak broad Balmer emission in the rest-frame optical spectra taken with the JWST-NIRSpec, suggests that they may be luminous counterparts to JWST-selected AGN, including LRDs, discovered at high redshifts. We interepret their weak broad Balmer emission and faint optical continua as a result of the BLRs being partly visible, while the rest of the BLRs, the optical continuum

and X-ray emitting regions of the accretion disc are hidden behind an optically-thick obscuring torus. Any X-ray emission can be suppressed if the obscuring matter is Compton-thick, due to the ISM of the host galaxies, as hypothesised and observed at high redshifts. Alternatively, an inflated inner accretion disc in a supercritical accretion flow could strongly suppress X-ray emission with an orientation effect.

Acknowledgements. We thank Shin Mineshige, Livia Vallini, Roberto Decarli for useful discussion, and Guido Risaliti for providing us with the data used for Fig. 8. The results reported in this article are based on observations made by the Chandra X-ray Observatory and made use of software provided by the Chandra X-ray Center (CXC). Support for this work was provided by NASA through Chandra Award Number 23700304 issued by CXC. KIw acknowledges support under the grant PID2022-136827NB-C44 provided by MCIN/AEI/10.13039/501100011033/FEDER, UE. MO acknowledges support from Japan Society for the Promotion of Science (JSPS) KAKENHI Grant Number 24K22894. YM was supported by the Japan Society for the Promotion of Science (JSPS) KAKENHI Grant No. 21H04494. KK acknowledges the support by JSPS KAKENHI Grant Numbers 22H04939, 23K20035, and 24H00004. RG and FV acknowledge financial support by the INAF Grants for Fundamental Research 2023.

References

Abramowicz, M. A., Czerny, B., Lasota, J. P., & Szuszkiewicz, E. 1988, ApJ, 332, 646
Aihara, H., Arimoto, N., Armstrong, R., et al. 2018, PASJ, 70, S4
Alexandroff, R., Strauss, M. A., Greene, J. E., et al. 2013, MNRAS, 435, 3306
Antonucci, R. R. J. & Miller, J. S. 1985, ApJ, 297, 621
Barvainis, R. 1987, ApJ, 320, 537
Berney, S., Koss, M., Trakhtenbrot, B., et al. 2015, MNRAS, 454, 3622
Bosman, S. E. I., Álvarez-Márquez, J., Colina, L., et al. 2024, Nature Astronomy, 8, 1054
Calhau, J., Sobral, D., Santos, S., et al. 2020, MNRAS, 493, 3341
Davies, F. B., Hennawi, J. F., & Eilers, A.-C. 2019, ApJ, 884, L19
Ding, X., Onoue, M., Silverman, J. D., et al. 2023, Nature, 621, 51
Elitzur, M. & Ho, L. C. 2009, ApJ, 701, L91
Fan, X., Strauss, M. A., Richards, G. T., et al. 2006, AJ, 131, 1203
Ferland, G. J., Done, C., Jin, C., Landt, H., & Ward, M. J. 2020, MNRAS, 494, 5917
Fruscione, A., McDowell, J. C., Allen, G. E., et al. 2006, in Society of Photo-Optical Instrumentation Engineers (SPIE) Conference Series, Vol. 6270, Observatory Operations: Strategies, Processes, and Systems, ed. D. R. Silva & R. E. Doxsey, 62701V
Furtak, L. J., Labbé, I., Zitrin, A., et al. 2024, Nature, 628, 57
Georgantopoulos, I. & Akylas, A. 2010, A&A, 509, A38
Gilli, R., Norman, C., Calura, F., et al. 2022, A&A, 666, A17
Greene, J. E. & Ho, L. C. 2005, ApJ, 630, 122
Greene, J. E., Labbe, I., Goulding, A. D., et al. 2024, ApJ, 964, 39
Haardt, F. & Maraschi, L. 1991, ApJ, 380, L51
Harikane, Y., Zhang, Y., Nakajima, K., et al. 2023, ApJ, 959, 39
Hashimoto, T., Ouchi, M., Shimasaku, K., et al. 2017, MNRAS, 465, 1543
Heckman, T. M., Ptak, A., Hornschemeier, A., & Kauffmann, G. 2005, ApJ, 634, 161
Hickox, R. C. & Alexander, D. M. 2018, ARA&A, 56, 625
Huang, J., Luo, B., Du, P., et al. 2020, ApJ, 895, 114
Inayoshi, K., Kimura, S., & Noda, H. 2024, arXiv e-prints, arXiv:2412.03653
Jiang, L., McGreer, I. D., Fan, X., et al. 2015, AJ, 149, 188
Jiang, Y.-F., Stone, J. M., & Davis, S. W. 2019, ApJ, 880, 67
Jin, C., Ward, M., & Done, C. 2012, MNRAS, 422, 3268
Juodžbalis, I., Maiolino, R., Baker, W. M., et al. 2024, Nature, 636, 594
Just, D. W., Brandt, W. N., Shemmer, O., et al. 2007, ApJ, 665, 1004
Kang, J.-L., Done, C., Hagen, S., et al. 2024, arXiv e-prints, arXiv:2410.06730
Kashikawa, N., Ishizaki, Y., Willott, C. J., et al. 2015, ApJ, 798, 28
Kaspi, S., Smith, P. S., Netzer, H., et al. 2000, ApJ, 533, 631
Kauffmann, G., Heckman, T. M., Tremonti, C., et al. 2003, MNRAS, 346, 1055
Kawanaka, N. & Mineshige, S. 2021, PASJ, 73, 630
Kawashima, T., Ohsuga, K., Mineshige, S., et al. 2009, PASJ, 61, 769
Kawashima, T., Ohsuga, K., Mineshige, S., et al. 2012, ApJ, 752, 18
King, A. 2024, MNRAS, 531, 550
Kitaki, T., Mineshige, S., Ohsuga, K., & Kawashima, T. 2017, PASJ, 69, 92
Kocevski, D. D., Finkelstein, S. L., Barro, G., et al. 2024, arXiv e-prints, arXiv:2404.03576
Konno, A., Ouchi, M., Nakajima, K., et al. 2016, ApJ, 823, 20
Kraft, R. P., Burrows, D. N., & Nousek, J. A. 1991, ApJ, 374, 344
Krawczyk, C. M., Richards, G. T., Mehta, S. S., et al. 2013, ApJS, 206, 4
Li, Z., Inayoshi, K., Chen, K., Ichikawa, K., & Ho, L. C. 2025, ApJ, 980, 36
Liu, T., Tozzi, P., Wang, J.-X., et al. 2017, ApJS, 232, 8
Loiacono, F., Decarli, R., Mignoli, M., et al. 2024, A&A, 685, A121
Lusso, E., Hennawi, J. F., Comastri, A., et al. 2013, ApJ, 777, 86
Lusso, E. & Risaliti, G. 2016, ApJ, 819, 154
Lusso, E., Risaliti, G., Nardini, E., et al. 2020, A&A, 642, A150
Maiolino, R., Risaliti, G., Signorini, M., et al. 2025, MNRAS, 538, 1921
Maiolino, R., Übler, H., Perna, M., et al. 2024, A&A, 687, A67
Malhotra, S. & Rhoads, J. E. 2002, ApJ, 565, L71
Malkan, M. A., Jensen, L. D., Rodriguez, D. R., Spinoglio, L., & Rush, B. 2017, ApJ, 846, 102
Marshall, M. A., Perna, M., Willott, C. J., et al. 2023, A&A, 678, A191
Marshall, M. A., Windhorst, R. A., Ferrami, G., et al. 2025, arXiv e-prints, arXiv:2502.20550
Matsuoka, Y., Iwasawa, K., Onoue, M., et al. 2019, ApJ, 883, 183
Matsuoka, Y., Iwasawa, K., Onoue, M., et al. 2018a, ApJS, 237, 5
Matsuoka, Y., Onoue, M., Iwasawa, K., et al. 2025, ApJ, submitted
Matsuoka, Y., Onoue, M., Kashikawa, N., et al. 2018b, PASJ, 70, S35
Matsuoka, Y., Onoue, M., Kashikawa, N., et al. 2016, ApJ, 828, 26
Matsuoka, Y., Strauss, M. A., Kashikawa, N., et al. 2018c, ApJ, 869, 150
Matthee, J., Naidu, R. P., Brammer, G., et al. 2024, ApJ, 963, 129
Miyazaki, S., Komiyama, Y., Kawanomoto, S., et al. 2018, PASJ, 70, S1
Mulchaey, J. S., Koratkar, A., Ward, M. J., et al. 1994, ApJ, 436, 586
Nakajima, K., Schaerer, D., Le Fèvre, O., et al. 2018, A&A, 612, A94
Nanni, R., Vignali, C., Gilli, R., Moretti, A., & Brandt, W. N. 2017, A&A, 603, A128
Ni, Y., Di Matteo, T., Gilli, R., et al. 2020, MNRAS, 495, 2135
Ogawa, T., Ohsuga, K., Makino, Y., & Mineshige, S. 2021, PASJ, 73, 701
Ohsuga, K. & Mineshige, S. 2007, ApJ, 670, 1283
Ohsuga, K., Mori, M., Nakamoto, T., & Mineshige, S. 2005, ApJ, 628, 368
Onoue, M., Ding, X., Silverman, J. D., et al. 2024, arXiv e-prints, arXiv:2409.07113
Onoue, M., Matsuoka, Y., Kashikawa, N., et al. 2021, ApJ, 919, 61
Osterbrock, D. E. 1962, ApJ, 135, 195
Osterbrock, D. E. 1977, ApJ, 215, 733
Rakshit, S., Stalin, C. S., & Kotilainen, J. 2020, ApJS, 249, 17
Schindler, J.-T., Hennawi, J. F., Davies, F. B., et al. 2024, arXiv e-prints, arXiv:2411.11534
Scoville, N., Lee, N., Vanden Bout, P., et al. 2017, ApJ, 837, 150
Shen, Y., Richards, G. T., Strauss, M. A., et al. 2011, ApJS, 194, 45
Shibuya, T., Ouchi, M., Harikane, Y., et al. 2018, PASJ, 70, S15
Sądowski, A., Narayan, R., Tchekhovskoy, A., et al. 2015, MNRAS, 447, 49
Sobral, D., Matthee, J., Darvish, B., et al. 2018, MNRAS, 477, 2817
Steffen, A. T., Strateva, I., Brandt, W. N., et al. 2006, AJ, 131, 2826
Stern, J. & Laor, A. 2012a, MNRAS, 426, 2703
Stern, J. & Laor, A. 2012b, MNRAS, 423, 600
Tadaki, K., Esposito, F., Vallini, L., et al. 2025, Nature Astronomy [arXiv:2503.07964]
Takahashi, H. R. & Ohsuga, K. 2015, PASJ, 67, 60
Trebitsch, M., Volonteri, M., & Dubois, Y. 2019, MNRAS, 487, 819
Trouille, L. & Barger, A. J. 2010, ApJ, 722, 212
Übler, H., Maiolino, R., Curtis-Lake, E., et al. 2023, A&A, 677, A145
Vignali, C., Brandt, W. N., & Schneider, D. P. 2003, AJ, 125, 433
Vito, F., Brandt, W. N., Bauer, F. E., et al. 2019, A&A, 630, A118
Vito, F., Brandt, W. N., Yang, G., et al. 2018, MNRAS, 473, 2378
Wang, B., Leja, J., de Graaff, A., et al. 2024, ApJ, 969, L13
Weisskopf, M. C., Wu, K., Trimble, V., et al. 2007, ApJ, 657, 1026
Willott, C. J., Delfosse, X., Forveille, T., Delorme, P., & Gwyn, S. D. J. 2005, ApJ, 633, 630
Willott, C. J., Delorme, P., Reylé, C., et al. 2009, AJ, 137, 3541
Winkler, H. 1992, MNRAS, 257, 677
Wu, X.-B., Wang, F., Fan, X., et al. 2015, Nature, 518, 512
Yue, M., Eilers, A.-C., Ananna, T. T., et al. 2024a, ApJ, 974, L26
Yue, M., Eilers, A.-C., Simcoe, R. A., et al. 2024b, ApJ, 966, 176
Zappacosta, L., Piconcelli, E., Fiore, F., et al. 2023, A&A, 678, A201